# High-pressure EXAFS measurements of solid and liquid Kr

A. Di Cicco
*Dipartimento di Matematica e Fisica, Università degli Studi di Camerino, Unità di Ricerca, Instituto Nazionale di Fisica della Materià, Via Madonna delle Carceri, 62032 Camerino (MC), Italy*

A. Filipponi
*European Synchrotron Radiation Facility, Boîte Postale 220, F-38043 Grenoble, France*

J. P. Itié and A. Polian
*Laboratoire de Physique des Milieux Condensés, Université Pierre et Marie Curie, T13 E4, 4 place Jussieu, F-75252 Paris Cedex 05, France*

(Received 8 April 1996)

X-ray-absorption measurements of liquid and solid krypton at room temperature in the pressure range 0.1–30 GPa have been performed using the dispersive setup and diamond-anvil cells as a pressure device. The evolution of the near-edge structures as a function of pressure, including the first intense resonance, has been interpreted using multiple-scattering calculations. It is shown that the near-edge structures are reproduced taking into account two-body and three-body terms associated with the first-neighbor atoms. Extended x-ray-absorption fine-structure (EXAFS) spectra have been analyzed in the framework a multiple-scattering data-analysis approach taking proper account of the atomic background including the $[1s4p]$, $[1s3d]$, and $[1s3p]$ double-electron excitation channels. Isobaric Monte Carlo (MC) computer simulations based on empirical pair potentials, as proposed by Barker (K2) and Aziz (HFD-B), have been performed to make a quantitative comparison of theoretical and experimental local structural details of condensed krypton at high pressures. From the analysis of EXAFS data we were able to obtain simultaneous information on average distance, width, and asymmetry of the first-neighbor distribution, as a function of pressure. These parameters yield a unique insight on the potential function because they are affected by both minimum position and curvature of the effective pair potential. The trend of the first-neighbor distribution as a function of pressure is in quantitative agreement with the HFD-B potential at moderate pressures, deviations are found at higher pressures where EXAFS spectra are very sensitive to the hard-core repulsive part of the potential. The weak EXAFS signal of liquid krypton at room temperature and 0.75 GPa has been found in accord with the results of the MC simulations within the noise of the measurement. [S0163-1829(96)06937-8]

## I. INTRODUCTION

Measurements of *K*-edge x-ray-absorption spectra of noble gases in a wide range of temperature and pressures deserve a large fundamental interest. The simplicity of the atomic electronic structure of these systems, which is almost unaffected in the solid or liquid phases, makes current approximations for the calculation of the x-ray-absorption signal quite reliable. Moreover, structural properties of noble gases in condensed phases are well known from diffraction experiments and can be accurately predicted by suitable simple empirical interatomic potentials. For these reasons, on the one hand, due to the reliability of the calculations, the theory of the x-ray-absorption spectroscopy (XAS) can be put to a severe test; on the other hand, it is conceivable that the analysis of the XAS data can provide additional reliable structural information. This is expected to be valuable especially for the short-range shape of the interatomic interaction. Among the noble gases the most suitable to perform XAS experiments is certainly Kr which is the subject of the present paper.

For noble gases the potential energy is accurately modeled by an expression of the type

$$U(q)=\sum_{(ij)} V^{(2)}(|q_i-q_j|)+\sum_{(ijk)} V^{(3)}(q_i,q_j,q_k)+\cdots, \tag{1}$$

where the main contribution is due to the irreducible two-body $V^{(2)}$ potential, while the three-body interaction is a small perturbation. Accurate expressions for the pair interaction, based on a wide range of experimental data, have been proposed. Several different potentials have been used for Kr, we will consider the K2 potential proposed by Barker *et al.*[1] and the HFD-B proposed by Aziz and Slaman.[2] The leading many-body correction is currently accepted to be accurately reproduced by the Axilrod-Teller-Muto[3] (ATM) triple-dipole functional form.

Accurate ensemble averaged structural properties can be calculated, from $U(q)$, by computer simulations or integral equation techniques and can be compared with available experiments. Neutron-diffraction (ND) measurements in the dense gas phase[4] were found in slight disagreement with the virial expansion and Monte Carlo (MC) simulation results[5] even after inclusion of the ATM term. Aers and Dharma-wardana[6] have shown instead a good agreement between ND data and hypernetted-chain calculations and also pointed out that the effect of ATM forces is expected to

 

decrease with increasing density. Barker[7] performed MC calculation for fluid Kr up to 0.03 mol/cm$^3$ density showing high accuracy in the pressure and internal energy predictions from a K2+ATM potential. Friedrikze[8] found instead that this potential cannot describe adequately his ND data along the subcritical and supercritical isotherms at 200 and 220 K. Calculations were performed using MHNC equations and molecular dynamics. More recently Barocchi and co-workers performed high precision ND measurements[9–11] of liquid Kr just above the coexistence curve that represent a severe test for the interaction potentials. Theoretical structure factors calculated with the MHNC equation using the theory developed by Reatto and Tau[12] have shown that inclusion of the ATM effective interaction reduces considerably the discrepancies with the experiment. The isothermal density derivative of the structure factor was found to be extremely sensitive to the potential models. In view of these results, the possibility to compare theoretical calculation with different experimental structural determination as those performed by XAS, possibly in a wide range of temperature and pressures, is thus extremely stimulating.

Several *K*-edge XAS measurements of atomic Kr in different phases have been reported. Various studies of x-ray-absorption spectra of gaseous Kr under low-pressure conditions, focused on the understanding of the threshold features from an atomic-physics standpoint, have been published since the advent of synchrotron radiation.[13–17] Differences between the XAS spectra of gaseous and solid Kr (at low temperature) were early recognized,[18] and the intense threshold features in the solid phase spectrum were reproduced by x-ray-absorption near-edge structure (XANES) multiple-scattering calculations and identified as resonances in the continuum.[19] A XAS investigation of solid Kr at room temperature, under high-pressure condition in the range from 1.6 to 20 GPa was previously performed with a diamond-anvil cell (DAC) and a dispersive setup.[20] A very intense first resonance (referred to as ''white line'' in the following) is observed and the analysis of the fine structure yielded structural results in agreement with both x-ray-diffraction and theoretical calculations. A study of two-dimensional condensed phase of Kr on *ZYX* graphite substrates was performed indicating large thermal fluctuations.[21] Differences in the extended x-ray-absorption fine structure (EXAFS) between the disordered and incommensurate phases were detected. A further experimental study was performed on ion-implanted Kr in solid matrices.[22] The typical XANES pattern suggested that at high dosages Kr precipitates into high-pressure bubbles.

Stimulated by the recent experimental advances in the high-pressure EXAFS technique and by the theoretical advances in the interpretation of the absorption cross section, we have undertaken a complete XAS experiment on high-pressure phases of Kr. The main experimental objective was to extend the pressure interval of the previous experiment[20] to include spectra of the liquid phase below 0.8 GPa and higher pressure solid phase spectra in an extended energy range. The maximum pressure that can be reached is, however, still below that of the predicted fcc to hcp and metallization transitions.[23]

From the XAS theory standpoint a quite interesting property of noble gases is that due to the weakness of the chemical bond it is possible to follow the gradual transition of the spectrum from that of an isolated atom to that of the atom embedded in a condensed medium at high density, for instance by increasing pressure. Under these conditions it is expected to be possible to follow the modification of the Kr spectrum associated with the gradual onset of a rigid first-neighbor cage. The use of an advanced multiple-scattering EXAFS data-analysis method has allowed us to retrieve reliable structural information on the short-range pair distribution function. Structural results as a function of pressure can be then compared with those derived from computer simulations and provide an unique tool to investigate the details of the interatomic potential. In particular, the results of a high-pressure XAS experiment are quite interesting since they provide further information on the inner repulsive core part of the pair interaction and can put to a test current approximations of the interatomic potential.

The paper is organized as follows: in Sec. II a description of the experimental details concerning measurements and preparation of samples is reported; in Sec. III the trend of the near-edge structures as a function of pressure is discussed in light of multiple-scattering calculations; in Sec. IV the proper modeling of the atomic background including double-electron excitation to be used in the EXAFS data analysis, is exposed; in Sec. V the results of constant pressure Monte Carlo simulations of high-pressure solid and liquid Kr are presented; in Sec. VI and in Sec. VII the results of the EXAFS data analysis on high-pressure and room-temperature solid and liquid Kr are discussed and compared with Monte Carlo simulations; finally, Sec. VIII is devoted to the conclusions.

## II. EXPERIMENTAL DETAILS

High-pressure x-ray-absorption measurements were performed using the dispersive setup and standard diamond-anvil cells as pressure devices. A diamond-anvil cell equipped with Ta gaskets was used for measurements in the range of pressures 0.1–8.0 GPa. A second anvil cell equipped with diamonds of smaller size and stainless steel gaskets was used for higher pressures in the range 8–30 GPa. The starting thickness of the inner region of the gaskets was about 50 $\mu$m. Pure krypton was loaded into the cell by condensation of gaseous Kr upon the diamonds maintained in direct contact with a liquid $N_2$ bath.

Kr *K*-edge EXAFS measurements have been recorded using the dispersive setup available at LURE and synchrotron radiation emitted by the DCI storage ring operating at 1.85 GeV with typical currents of 300 mA (beamline D11).[24] Particular care was adopted to improve the quality and energy extension of the spectra. Appearance of strong Bragg peaks from the diamonds was avoided by optimizing the position of the cell and of the two diamonds.

Measurements covered the pressure range 0.1–30 GPa at room temperature. Pressure was measured before and after each EXAFS scan by using the standard ruby-fluorescence technique.[25]

The liquid-solid phase transition takes place at 0.847 GPa at 300 K.[26] Several low-noise measurements at different pressures were recorded for liquid Kr between 0.1 and 0.75 GPa and for solid krypton above about 1.2 GPa. Previous

measurements had been performed in a narrow energy region and only for solid Kr in the range of pressures between 1.6 and 20 GPa.[20]

In the present case, the larger size of the krypton sample used for measurements in the range 0.1–8 GPa allowed us to perform accurate EXAFS measurements at lower pressures. The available energy range was also extended to about 300 eV above the Kr $K$ edge. Low-noise spectra were obtained by summing 60 spectra (1024 pixel data), each one recorded with a total integration time of about 14 s. Accurate measurements of the x-ray-absorption coefficient of gas-phase Kr were also performed both using the dispersive setup and in transmission mode using a conventional channel-cut (331) monochromator (beamline D42 at LURE). Signal-to-noise ratios of about $10^3$ and 5 x $10^4$ were attained for high-pressure spectra and gas-phase experiments, respectively.

Measurements of the atomic background are particularly important for reliable studies of the x-ray-absorption fine structure in condensed phases. In fact, the gas-phase (atomic) Kr $K$-edge absorption coefficient shows well-defined and intense features due to double-electron channels. In our case, the atomic background has been also used to determine the calibration of the photon energy scale. The atomic background recorded on the 1024 pixel scale (dispersive setup) has been reproduced by means of a fitting program using as a model the same gas-phase spectrum recorded scanning the photon energy with the (331) channel-cut monochromator (beamline D42). The strong resonance due to the $[1s4p]$ double-electron shake-up channel and the other features due to the $[1s3d]$ and $[1s3p]$ channels, discussed in Sec. IV, allowed us to define the energy scale up to 300 eV above the edge in a very accurate way. The energy scale resulted to be almost linear as a function of the pixel number: $E=a+bn+cn^2+dn^3$, where $a=14225.4$ eV, $b=0.8611$ eV, $c=-0.3153\times10^{-4}$ eV, $d=0.4162\times10^{-7}$ eV. The accuracy of the energy scale was also verified by looking at the Au $L_1$ EXAFS of pure gold recorded after each scan and can be estimated to be better than 2 eV in the region of EXAFS spectra under consideration. The relative accuracy of the energy scale of the EXAFS signals recorded at different pressures is estimated to be better than 1 eV.

In Fig. 1 x-ray-absorption measurements of gaseous Kr (lower curve), liquid Kr between 0.1 and 0.75 GPa (starting from the lower curve), and solid Kr (upper curves) are shown. A spectacular trend of the edge features is observed, as a function of pressure. The liquid-solid transition, monitored during the experiment using an optical microscope, is clearly associated with an increase of the EXAFS intensity in the absorption signal. The characteristic white line appears, and increases as a function of pressure, in condensed phases. This feature is *absent* in gaseous Kr as is well known.[18,19,22] In the next section we discuss the fine structure of the near-edge absorption spectra in the framework of the multiple-scattering theory.

## III. NEAR-EDGE STRUCTURE IN Kr CONDENSED PHASES

The evolution of the absorption spectra reported in Fig. 1 shows that an intense white line grows up at the $K$-edge energy threshold as a function of pressure in the condensed phases. The EXAFS oscillations are very weak at low pressures therefore the edge features are the most sensitive signatures in the x-ray-absorption spectra for local ordering in condensed Kr.

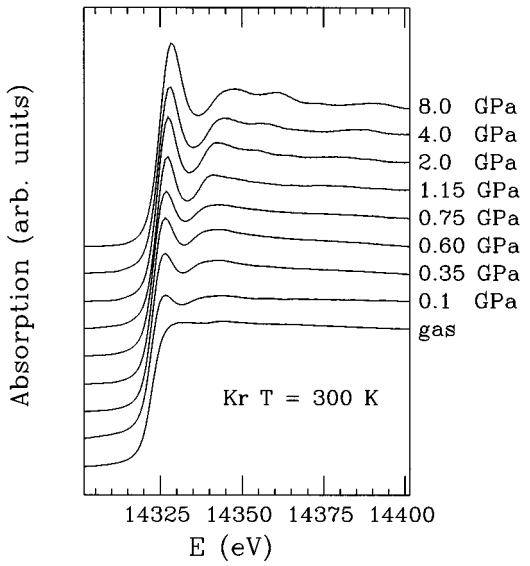


FIG. 1. $K$-edge XAFS spectra of gaseous (lower curve), liquid (0.1–0.75 GPa), and solid Kr as a function of pressure at room temperature.

The near-edge structures were calculated by using multiple-scattering (MS) theory within the one-electron and muffin-tin approximations. In this case, due to the absence of covalent bonding and to the large interatomic distances, the muffin-tin approximation is expected to be very accurate.

The cross section was calculated according to the usual expression[27,28] of the polarization averaged cross section valid for transitions to a dipole selected final state, using the continued-fraction expansion[29] method. Phase-shift matrix $T$ was evaluated using a Hedin-Lundqvist complex exchange-correlation self-energy accounting for inelastic losses of the photoelectron.[30]

The $K$-edge x-ray-absorption cross section was initially calculated for face-centered solid Kr at about 8 GPa with interatomic distances derived from previous diffraction measurements. Cluster of 13, 19, 43, and 55 atoms including the first, second, third, and fourth shell, respectively, were used for MS calculations. We verified, in agreement with previous findings,[19] that the near-edge structure calculations converge rapidly and the asymptotic behavior is readily obtained using the smaller cluster with only first neighbors. We used different real and complex exchange-correlation potentials and different nonoverlapping muffin-tin radii obtaining always similar results. In particular, the white line is simply obtained including the first-neighbor environment. The appearance of the white line is due to a multiple-scattering resonance related to the rapid variation of the $l=0$ phase-shift $\delta$ near $\pi/2$ just above the $K$ threshold.[31]

In Fig. 2 the $K$-edge x-ray absorption cross section calculated using MS theory is reported (solid line). The MS calculations shown in Fig. 2 were performed including only first neighbors at a distance of 3.40 Å. Core-hole 1$s$ width (full width 2.34 eV, see Ref. 32) and experimental broadening

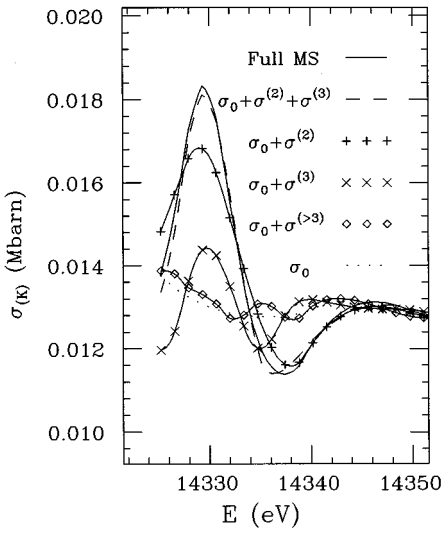


FIG. 2. *K*-edge x-ray absorption cross section calculated using multiple-scattering theory. The full multiple-scattering calculation (Full MS, solid line) is able to reproduce the characteristic white line observed in Kr condensed phases. The atomic *K*-edge one-electron cross section $\sigma_0$ is also shown (dotted curve). The two-body $\sigma_0 + \sigma^{(2)}$, three-body $\sigma_0 + \sigma^{(3)}$ and higher-order $\sigma_0 + \sigma^{(n>3)}$ partial cross sections are reported showing the rapid convergence of the *n*-body expansion. The $\sigma_0 + \sigma^{(2)} + \sigma^{(3)}$ cross section (dashed) approaches that calculated using all of the *n*-body configurations.

(total width of about 3 eV) were also considered. The full multiple-scattering calculation (full MS, solid line) is clearly able to reproduce the characteristic white line observed in Kr condensed phases.

The full MS calculation contains the multiple-scattering contributions of any order related to the position of all of the atoms of the cluster. A deeper insight on the relationship between the atomic structure and the x-ray-absorption cross section can be obtained using the irreducible *n*-body partial cross sections $\sigma^{(n)}$.[28] Indicating with $\sigma^{(1)}(0)=\sigma_0$ the absorption cross section due to the presence of a the single photoabsorber atom 0 (atomic cross section), then the two-body cross section associated with the presence of the atom *i* is

$$\sigma^{(2)}(0,i)=\sigma(0,i)-\sigma^{(1)}(0). \tag{2}$$

In an analogous way, the irreducible three-body contribution associated with the simultaneous presence of the atoms *i* and *j* is defined by

$$\sigma^{(3)}(0,i,j)=\sigma(0,i,j)-\sigma^{(2)}(0,i)-\sigma^{(2)}(0,j)-\sigma^{(1)}(0). \tag{3}$$

In general, for a cluster of $n+1$ atoms the total cross section $\sigma(0,i,j,\ldots,n)$ can be written using an useful expansion in terms of the irreducible *n*-body cross sections:

$$\sigma(0,i,j,\ldots,n)=\sigma_0+\sum_i \sigma^{(2)}(0,i)+\sum_{(i,j)} \sigma^{(3)}(0,i,j) + \sum_{(i,j,k)} \sigma^{(4)}(0,i,j,k)+\cdots + \sigma^{(n)}(0,i,j,\ldots,n). \tag{4}$$

An important characteristic of the *n*-body expansion of Eq. (4) is that due to the fast convergence only a few low-order terms are usually sufficient. It has been shown[28] that the convergence of this series is never worse than that of the corresponding multiple-scattering expansion while, in addition, a more clear physical assignment of the features can be performed.

In solid Kr, the convergence of the *n*-body expansion is fast and $n>3$ terms give a negligible contribution to the x-ray-absorption cross section. In Fig. 2 the partial two-body $\sigma_0 + \sigma^{(2)}$, three-body $\sigma_0 + \sigma^{(3)}$, and higher-order $\sigma_0 + \sigma_{(n>3)}$ cross sections are reported showing the rapid convergence of the *n*-body expansion. The $\sigma_0 + \sigma^{(2)} + \sigma^{(3)}$ cross-section (dashed) including only the two-body and three-body contributions approaches that calculated using all of the *n*-body configurations. The higher-order $\sigma_0 + \sigma_{(n>3)}$ cross section follows substantially the underlying atomic *K*-edge one-electron cross section $\sigma_0$.

Figure 2 shows that MS two-body and three-body terms are sufficient to explain near-edge structures of solid Kr. In practice, even the white line is mainly due to the partial two-body cross section $\sigma^{(2)}$, associated with a single structural parameter: the interatomic distance. The $\sigma^{(3)}$ cross section can be also decomposed into partial contributions associated with different triangular configurations found in the fcc first-neighbor structure (see Sec. VI). However, all of these configurations give x-ray-absorption signals of similar intensity and they can hardly be decoupled.

The calculated x-ray-absorption cross section shows a reasonable quantitative agreement with the experimental data. In Fig. 3 the near-edge experimental data of solid Kr are compared with full MS calculations. Results are presented as a function of pressure and the overall agreement between calculations and experimental data is good. These calculations were carried out using constant muffin-tin radii and nearest-neighbor distances of about 3.85, 3.75, 3.61, and 3.40 Å obtained from the cell sizes derived from previously published x-ray-diffraction and absorption experiments at about 1.15, 2, 4, and 8 GPa, respectively. A clear trend of the near-edge structure is observed as a function of pressure.

A continuous regular change in the energy position of the white line and a more visible shift of the second peak (see Fig. 3) are found increasing the pressure. The change in the energy position of the maxima and minima of the fine structure is directly related to the variation of the interatomic distances through the spherical-wave propagator matrix *G* appearing into the expression of the MS absorption cross section (inversion of the matrix $I-GT$). A second interesting feature is the increase of the white-line intensity as a function of pressure. This phenomenon has a less straightforward explanation but can be still reproduced by MS calculations shown in Fig. 3.

The energy shift found by increasing the pressure can be

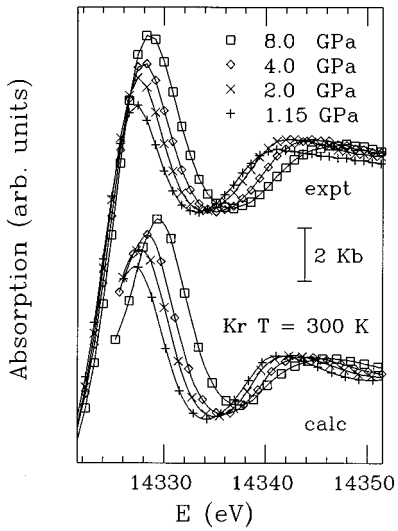


FIG. 3. Full MS calculations (calc) compared with near-edge experimental data of solid Kr (expt) as a function of pressure. Agreement between calculations and experimental data is good. The trend of the intensity of the white line is reproduced only when phase shifts are calculated for the actual interatomic distances. The experimental cross section at high energies ($E>14\,340$ eV) is higher due to the double-electron channel $[1s4p]$ contribution.

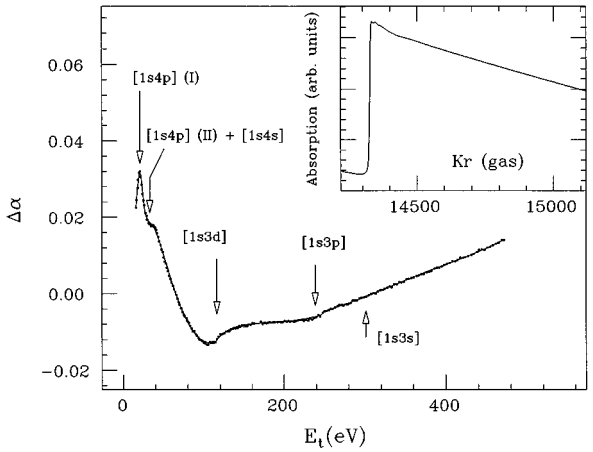


FIG. 4. Absorption $K$-edge excess $\Delta\alpha$ as a function of the energy above the threshold $E_t$ in gaseous Kr. Arrows refer to the thresholds for shake-up channels involving the additional excitation of $4p$, $4s$, $3d$, $3p$, and $3s$ electrons, respectively (see text). The original gas-phase Kr $K$-edge absorption spectrum is shown in the inset.

simply accounted for by changing the interatomic distances in the propagator matrix $G$. Conversely, the increase of the intensity of the white line can be obtained only when phase shifts (matrix $T$) are calculated each time using the actual interatomic distances. The increase of the intensity of the white line in the MS calculations is due to the slight change in the phase shifts, due to the increased overlap of the 12 nearest-neighbor atomic charge-density tails following the contraction of the interatomic distances. A slight change in the phase shift $l=0$ curve produces visible changes in the cross section near the resonance. As a result, the cross section near a multiple-scattering resonance is more sensitive to the details of the atomic potential and the fact that the present muffin-tin potential is able to reproduce the trend in the intensity of the white line is a proof of the accuracy of this approximation in the present case. Of course, the sensitivity of the x-ray-absorption cross section to the details of the potential (phase shifts) is certainly less important at higher energies, in the EXAFS energy region where a reliable quantitative data analysis can be performed.

## IV. ATOMIC BACKGROUND: GASEOUS KRYPTON

As it has been pointed out in many recent papers, a reliable extraction of the EXAFS structural signal can be carried out only after performing a careful determination of the atomic background.[33] In fact, atomic background has been often found to be affected by anomalies associated with the opening of double-electron excitation channels.

Noble-gas spectra, being the most simple and tractable cases, were accurately studied. In particular, $K$-edge x-ray-absorption spectrum of atomic Kr has been studied by several scientists in the last ten years.[14–17] Well-defined features associated with core-level double-electron excitation channels have been identified by several groups. Calculated intensities and shape of the double-electron channels are reported in Ref. 17.

In Fig. 4 the $K$-edge absorption spectrum of gaseous krypton is shown in a large energy interval (inset). Features associated with the opening of the double-electron excitation channels are evidenced in the magnified plot shown in Fig. 4 reporting the dimensionless absorption excess $\Delta\alpha$ as a function of the energy above threshold $E_t$ (defined by the inflection point of the absorption, $E_e=14\,323$ eV). $\Delta\alpha$ is calculated subtracting an average linear decay from the absorption spectrum $\alpha(E)$ fitted in the EXAFS region, and normalized to the $K$-edge discontinuity.

Arrows in Fig. 4 indicate calculated excess energies required to excite additional electrons leaving double-hole $[1s4p]$, $[1s4s]$, $[1s3d]$, $[1s3p]$, and $[1s3s]$ configurations on the Kr atom. Clearly, arrows in Fig. 4 are in agreement with the visible anomalies of the atomic Kr absorption spectrum.

The onset excitation energies were calculated by differences of total energies of the atom in $[1s]$ single-hole and double-hole configurations. Total-energy calculations were performed using a relativistic self-consistent scheme.[34] Energies of the onsets were obtained starting from shake-up configurations where the additional electron is promoted from a specified core level to the first empty level with the same angular momenta $l$ and $j$, following the same procedures used in Refs. 35 and 36. For example, in the $[1s_{1/2}4p_{3/2}]$ case, the $4p_{3/2}$ electron is promoted into the first available $p$ state ($5p_{3/2}$). The onset energies are reported in Table I and provide an estimate of the lowest energy required to promote the second electron in the presence of the $1s$ core hole. Energy values are in substantial agreement with previous calculations reported in Ref. 14. However, features associated with the opening of the double-electron channels are usually spread over energy regions of about 5–20 eV around the shake-up threshold due to multiplet splitting and to the opening of the shake-off transitions.

As discussed in Ref. 17 the Kr $[1s4p]$ cross section ex-

TABLE I. Differences of total-energy calculations between excited shake-up states and $K$-edge continuum threshold for Kr ($Z=36$) based on Dirac-Fock total-energy calculations. All energies are in eV.

| $\Delta E(4p_{3/2})$ | $\Delta E(4p_{1/2})$ | $\Delta E(4s_{1/2})$ | $\Delta E(3d_{5/2})$ | $\Delta E(3d_{3/2})$ | $\Delta E(3p_{3/2})$ | $\Delta E(3p_{1/2})$ | $\Delta E(3s_{1/2})$ |
|---|---|---|---|---|---|---|---|
| 20.3 | 21.1 | 33.4 | 115.2 | 116.7 | 233.8 | 242.7 | 301.1 |

hibits a resonance structure at about 14 345 eV associated with bound to bound $1s->np$, $1s->n'p$ transitions [indicated as $[1s4p]$ (I) in Fig. 4]. Above this resonance structure, the double-electron cross section rises due to the contribution of the $[1s4s]$ and $[1s4p]$ (II) shake-up and shake-off transitions (see Fig. 4). The $[1s3d]$ and $[1s3p]$ channels show no resonant structures, but the rising of the cross section and their typical shape is evidenced in Fig. 4. The slight slope change observed in $\Delta\alpha$, hardly visible on the scale of Fig. 4, is assigned to the $[1s3s]$ contribution.

The atomic absorption shown in Fig. 4 can be modeled using simple empirical functions describing the shape of the double-electron channels and a polynomial spline accounting for the pre-edge and post-edge one-electron background contribution. The model curve is the solid line in Fig. 4 and reproduces the experimental $\Delta\alpha$ pattern within the statistical error. This background shape is transferable to the liquid and solid Kr absorption spectra. Its use is essential to determine the structural signal with reasonable accuracy because, especially for low pressures, the intensity of the double-electron features is of the same order of magnitude of the EXAFS oscillations. The background parameters were individually refined for each spectrum of solid and liquid Kr but the same pattern of discontinuities found for gas-phase Kr was maintained. No significant differences in the energy values were found while the magnitude of the discontinuities, instead, was found to vary slightly as a function of pressure. This may reflect changes in the double-electron excitation cross sections due to the induced modifications in shake-up final-state orbitals.

The bound to bound $[1s4p]$ (I) feature was modeled using a Lorentzian function of the photon energy $E$:

$$J_l \frac{1}{1+[(E-E_l)/\Delta E_l]^2}. \tag{5}$$

Best-fit values in gas-phase Kr were found to be $J_l = 0.021$ (3), $E_l = 14\,344(1)$ eV, $\Delta E_l = 6(1)$ eV. A 2% height of the bound to bound feature relative to the $K$ discontinuity is in good agreement with the calculation reported in Ref. 17 if the energy resolution of the monochromator is taken into account (total width of about 3 eV).

The second feature associated with the $[1s4s]$ and $[1s4p]$ (II) shake-up and shake-off transitions was modeled using an arctangent function

$$J_a\left[\frac{\arctan[(E-E_a)/\Delta E_a]}{\pi}+\frac{1}{2}\right]. \tag{6}$$

Best-fit values were found to be $J_a=0.035(5)$, $E_a=14\,355(5)$ eV, $\Delta E_a=9(2)$ eV.

The third and fourth features associated with the $[1s3d]$ and $[1s3p]$ channels, respectively, show well-defined discontinuities and were simulated using a steplike function of the type:

$$J_q\left(1-\frac{8}{3}\frac{E-E_q}{E_q}\right)\left[1-\left(\frac{\Delta E_q}{E-E_q+\Delta E_q}\right)^2\right]\theta(E-E_q). \tag{7}$$

where $\theta$ is the Heaviside function: $\theta(E-E_q)=0$, $(E-E_q)<0$; $\theta(E-E_q)=1$, $(E-E_q)\geq 0$.

The function (7) is able to reproduce the shape of the $[1s3d]$ and $[1s3p]$ absorption channels in the vicinity of the threshold in a quite accurate way. Best-fit values were $J_q=0.010(5)$, $E_q=14\,435(10)$ eV, $\Delta E_q=40(20)$ eV and $J_q=0.001(1)$, $E_q=14\,570(20)$ eV, $\Delta E_q=10(5)$ eV for the $[1s3d]$ and $[1s3p]$ channels, respectively. The asymptotic behavior of the double-electron absorption channels at high energies and the $[1s3s]$ contribution are easily reproduced by the polynomial spline and are not taken explicitly into account in the background model.

## V. LOCAL STRUCTURE OF CONDENSED KRYPTON: COMPUTER SIMULATIONS

A deep insight into atomic interaction potential and structure of a condensed system can be gained by comparing experimental determinations with theoretical calculations. In particular, comparison of results obtained using computer simulations and XAS can be very useful to investigate short-range structural properties. In the specific case of noble gases, including Kr, the very reliable existing potentials can be used to model the structure of condensed phases. A large number of investigations have been performed in the past in a wide range of thermodynamic conditions, both using computer simulations and integral equation techniques.[4–10] In the present study we performed a series of constant-pressure classical Monte Carlo (MC) simulations in configuration space covering the region investigated by the experiment. This specific simulation technique was chosen because EXAFS probes only equal time structural properties which are correctly sampled in the $(N,P,T)$ ensemble in this way. Quantum corrections are negligible in the investigated range. The reason to undertake specific simulations was due to the fact that we wanted to focus on several structural observables that are seldom taken into consideration. Moreover, specific simulations can be performed at exactly the same $P,T$ values as the experiment. Present simulations are based on pair potentials. While the limitations of these models are well known[4–10] they represent a firm reference for comparison with experimental data. The differences between simulations based on pair potential and experiments can then be ascribed to the effect of higher-order potential terms.

### A. Technique

Techniques for performing MC simulation in the $(N,P,T)$ ensemble are well established[37] and are based on the random sampling of the configurational space with the weight

$$\exp[-W(q,a;P,T)]=\exp[-\beta U(q,a)-\beta PV], \quad (8)$$

where $\beta=1/k_BT$, $U(q,a)$ is the internal energy, function of the particle coordinates $q$ and lattice parameter $a$, $P$ is the pressure, and $V=N_ca^3$ is the total box volume. In the present case we used a cubic box with periodic boundary conditions containing 500 or 864 atoms (with $N_c=5^3$ or $6^3$) and fcc cells.

The cubic lattice parameter $a$ is a random scaling variable subject to the MC random process like the atomic positions are. At each step first a particle movement is performed with standard Metropolis algorithm then a lattice parameter adjustment is attempted. The latter affects both $V=N_ca^3$ and $U$. In the present case, for a general pair interaction, no simple scaling procedures[37] can be applied and in principle all the interactions need to be recalculated, which is a time consuming process. In practice we approximate the function

$$\begin{aligned}\Delta W &= W_{(a+\delta)}-W_a=\beta PN_c[(a+\delta)^3-a^3]\\ &\quad+\beta[U(a+\delta)-U(a)]\\ &\approx \beta PN_c[(a+\delta)^3-a^3]+\beta(\partial U/\partial a)\,\delta \end{aligned} \quad (9)$$

and we calculate the derivative of the internal energy with respect to $a$, for a pairwise addictive potential, as

$$\frac{\partial U}{\partial a}=\sum_{(ij)}\left.\frac{\partial U_{(ij)}(r)}{\partial r}\right|_{r=r_{ij}}\frac{\partial r_{ij}}{\partial a}=\sum_{(ij)}\left.\frac{\partial U_{(ij)}(r)}{\partial r}\right|_{r=r_{ij}}\frac{r_{ij}}{a}. \quad (10)$$

The latter sum is calculated and updated at every particle move requiring only a constant fraction of additional time with respect to the internal energy update. The box size readjustment is accepted if $\Delta W\leqslant 0$, and is accepted with probability $\exp[-\Delta W]$ if $\Delta W>0$, as usual. In Eq. (10) there is no term proportional to the logarithm of the volume ratio because our particle displacements are in actual distance and not in the scaled variables. The maximum step sizes at each move were in the 0.1 Å range for the particles displacements and 0.001 Å for $a$. This latter value guarantees that the linear expansion in Eq. (9) is accurate. Typical acceptance rates fractions where in the 0.3–0.6 range for the particle and 0.95–0.99 range for the box readjustments.

Simulations have been performed starting both with fcc and disordered initial conditions. Energy, box size $a$, and the structure factor indicator for the main fcc reflection

$$S(111)=1+\frac{2}{N}\sum_{(ij)}\cos\left[\frac{2\pi}{a}(dx_{ij}+dy_{ij}+dz_{ij})\right], \quad (11)$$

were continuously monitored during the simulation to check equilibration and the possible onset of melting or crystallization. For fixed atoms in the fcc lattice $S(111)=N$, a small Debye-Waller decrement is obtained in the presence of thermal vibrations, however, for a fluid $S(111)$ fluctuates around unity. Normally around 100 000 moves were sufficient for equilibration apart from the region around the melting transition.

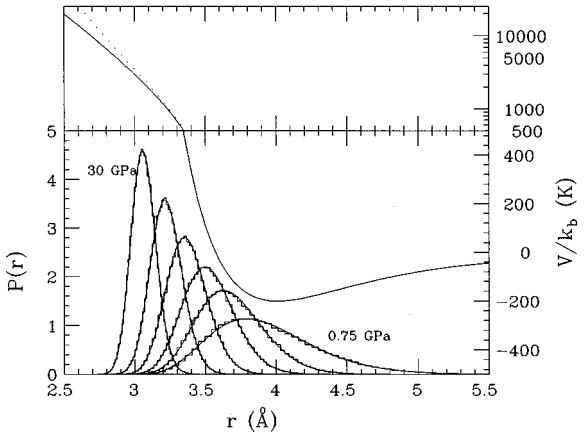


FIG. 5. Upper right diagrams: potential curves for the HFD-B (Ref. 2) (solid line) and K2 (Ref. 1) (dashed line) pair interaction. They differ mainly in the hard-core repulsive part shown on a logarithmic scale. Lower left diagram: On the same distance scale, first-neighbors bond-length probability distributions obtained from the simulations of solid Kr at 300 K as a function of pressure at 30, 15, 8, 4, 2, and 0.75 GPa (HFD-B potential). The latter curve is for a superheated solid.

Two different empirical potentials have been used for the simulations as proposed by Barker *et al.*[1] (K2) and by Aziz and Slaman[2] (HFD-B). These potentials represent quite reliably the pair interaction in a wide range of phases and atomic densities. They are substantially indistinguishable above 3.4 Å whereas they differ considerably in the repulsive hard-core region as shown in Fig. 5. The HFD-B potential has a slightly softer core. As pointed out by Barocchi *et al.*[9–11] the two potentials predict indistinguishable structures for the fluid measured in neutron-scattering experiment performed in a relatively low-pressure regime. In the present high-pressure experiments instead the atoms are confined at close enough distance to probe the repulsive hard-core region. Thus the comparison between high-pressure experiments and computer simulations can provide an insight into the nature of the repulsive forces.

### B. Simulation results

MC simulations have been performed at the temperature of 300 K and in a wide pressure range as indicated in Table II both starting from the ordered and disordered initial conditions. Spontaneous melting of the fcc lattice is directly observed for pressures below about 0.5 GPa. On the other hand spontaneous crystallization was not observed even at 4 GPa for up to $5\times10^5$ moves. Several observables were monitored during the simulation, including those probed by EXAFS spectroscopy. These were the average cell size $a$, the displacement distribution of atoms from the average lattice site, the bond length distribution of the first five neighbors, the triplet distributions among atoms connected by first-neighbor bonds at equilibrium angles of 60, 90, 120, and 180°. For each shell distribution, and in particular for the first shell, the first three cumulants have been calculated. These include the

TABLE II. MC simulation with the HFD-B potential (Ref. 2), parameters and results. The simulation temperature is 300 K, the successive columns report simulation pressure, initial conditions (fcc or random), resulting lattice parameter, density, average energy per atom $u$, fcc order parameter, mean-square displacement, and first-shell parameters $R$, $\sigma^2$, and $\beta$. For simulations that resulted in a fluid system $a$ refers to the appropriate fraction of the average simulation box size and $S(111)$ is replaced by the maximum of the structure factor $S(k)$.

| $P$ (GPa) | IC | $a$ (Å) | $\rho$ (nm$^{-3}$) | $u/k_B$ (K) | $S(111)$ | $\langle u_x^2\rangle$ ($10^{-3}$Å$^2$) | $R$ (Å) | $\sigma^2$ ($10^{-3}$Å$^2$) | $\beta$ |
|---|---|---|---|---|---|---|---|---|---|
| 30.0 | fcc | 4.3273 | 49.36 | 12700 | 481.4 | 5.93 | 3.063 | 7.64 | 0.18 |
| 25.0 | fcc | 4.3878 | 47.35 | 10405 | 478.2 | 7.04 | 3.107 | 8.79 | 0.19 |
| 20.0 | fcc | 4.4614 | 45.05 | 8071 | 476.6 | 8.41 | 3.159 | 10.4 | 0.19 |
| 15.0 | fcc | 4.5532 | 42.38 | 5736 | 472.6 | 10.1 | 3.225 | 12.6 | 0.21 |
| 12.0 | fcc | 4.6269 | 40.38 | 4262 | 465.8 | 12.9 | 3.278 | 15.4 | 0.25 |
| 10.0 | fcc | 4.6843 | 38.91 | 3299 | 462.9 | 14.3 | 3.320 | 17.2 | 0.27 |
| 8.0 | fcc | 4.7560 | 37.18 | 2317 | 456.9 | 17.1 | 3.372 | 20.8 | 0.29 |
| 6.0 | fcc | 4.8452 | 35.17 | 1368 | 445.3 | 21.9 | 3.437 | 26.6 | 0.35 |
| 4.0 | fcc | 4.9692 | 32.60 | 384 | 434.7 | 27.0 | 3.527 | 33.7 | 0.34 |
| 2.0 | fcc | 5.1778 | 28.81 | −529 | 408.9 | 46.8 | 3.683 | 56.8 | 0.45 |
| 1.2 | fcc | 5.3341 | 26.35 | −829 | 373.3 | 69.1 | 3.805 | 87.8 | 0.57 |
| 0.75[a] | fcc | 5.4807 | 24.30 | −938 | 308.3 | 120.0 | 3.929 | 140.0 | 0.73 |
| 0.35 | fcc | 5.8645 | 19.83 | −812 | 2.21 | | | | |
| 0.1 | fcc | 6.3546 | 15.59 | −719 | 1.71 | | | | |
| 4.00 | rand. | 5.0398 | 31.25 | 792 | 3.33 | | | | |
| 2.00 | rand. | 5.2629 | 27.44 | −221 | 3.26 | | | | |
| 1.20 | rand. | 5.4347 | 24.92 | −575 | 2.98 | | | | |
| 0.75 | rand. | 5.6025 | 22.75 | −717 | 2.57 | | | | |
| 0.35 | rand. | 5.8696 | 19.78 | −798 | 2.22 | | | | |
| 0.20 | rand. | 6.0924 | 17.69 | −764 | 1.93 | | | | |
| 0.10 | rand. | 6.3482 | 15.64 | −710 | 1.74 | | | | |

[a]Super-heated solid.

average distance $R$, the bond distance variance $\sigma^2$, and the skewness $\beta=\langle(r-R)^3\rangle/\sigma^3$. The main results are reported in Table II for the various simulations; notice that the statistical uncertainty is typically in the last digit (last two digits for $a$).

The bond length distribution obtained at different pressures for the HFD-B potential is shown in Fig. 5. The effect of the pressure on the distribution is quite evident. Upon releasing pressure the distribution broadens, shifts to higher distances, and becomes more asymmetric. At high pressure a considerable part of the atoms lays in the distance range where the difference between the two potential models (plotted on the same distance scale in Fig. 5) becomes important.

The results of the lattice spacing $a$ are reported in Table II and visualized in Fig. 6 on a logarithmic pressure scale. The difference between the two potential models amounts to about 0.1 Å at 30 GPa. The discontinuity between fluid and solid Kr is clearly evidenced in the plot. The simulation allows us to follow both phases in a relatively broad region around the melting transition. In the lower pressure range (below 10 GPa) the calculated cell size is slightly shortened with respect to the experimental values.[38,39] This discrepancy is similar to that found in liquid Kr in the comparison of $g(r)$ data from neutron diffraction with calculation based on the HFD-B pair potential and is assigned to the presence of higher-order interactions. It is generally assumed that the leading many-body interaction is repulsive and can be represented by the ATM triple-dipole model. At high pressure the discrepancy with x-ray-diffraction values[39,40] disappears indicating that for short distances the repulsive pairwise additive hard core dominates.

The parameters of the first-shell bond-length distribution are also reported in Table II as a function of pressure. In the next section, these values will be compared with those obtained by EXAFS showing that useful information on the nature of the interatomic forces can be obtained.

## VI. EXAFS DATA ANALYSIS OF SOLID KRYPTON

EXAFS spectra of solid krypton at room temperature in a wide range of pressure have been analyzed using multiple-scattering calculations and taking into account double-electron contributions in the background (see Sec. IV) in the framework of the GNXAS data-analysis method.[41,28] Details on the method and on its application to molecular and crystalline systems can be found in Refs. 41, 28, and 42.

The first four three-body and two-body configurations found in the fcc structure (see Table VI in Ref. 42) have been considered and the relevant $\gamma^{(2)}$ (two-body) and $\gamma^{(3)}$ (three-body) multiple-scattering signals calculated. Fitting of the raw data has been performed using the 60, 90, 120, and 180° triplet configurations including two first-neighbor distances, similarly to the other fcc case (Pd) previously presented.[42] In the present case, the fitting was performed with a total of 16 parameters (14 structural) over about 230 experimental energy points: first-neighbor distribution de-

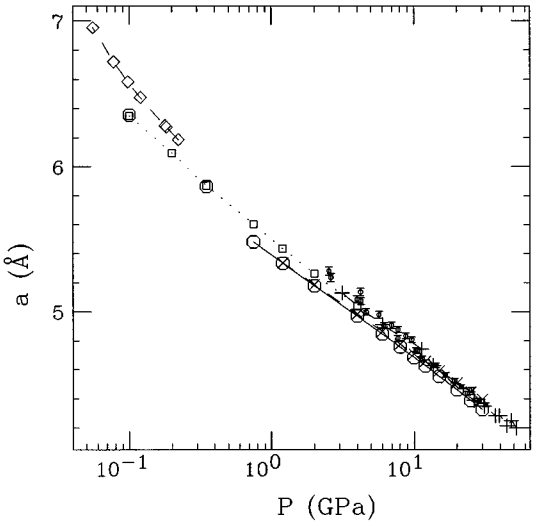


FIG. 6. Lattice spacing of solid Kr (fcc) as a function of pressure, as calculated by present simulations with the HFD-B (Ref. 2) (○) and K2 (Ref. 1) (×) potentials. Data joined by solid and dashed lines refer to solid Kr. Data points joined by a dotted line refer to fluid Kr, melted from fcc (○) or obtained from disordered initial conditions (□). Experimental values of the average spacing $a$ for liquid (◇) (Ref. 38) and solid krypton at high pressures, in the range 2–30 GPa (values shown with error bars) (Ref. 39) and in the range 3–40 GPa (+) (Ref. 40) are also reported. The slight deviation observed below 10 GPa indicates the presence of repulsive many-body forces that become less effective at high pressure.

fined by distance, variance, and skewness ($R$, $\sigma^2$, $\beta$); 60° triplet distribution defined by an additional bond-bond correlation $\rho_{r,r'}$; 90° triangles and second neighbors defined by the angle, angle variance, bond-bond, and bond angle correlations ($\theta_{90}$, $\sigma^2_{\theta_{90}}$, $\rho_{r,r''}$, $\rho_{r,\theta_{90}}$); 120° triangles and third shell ($\theta_{120}$, $\sigma^2_{\theta_{120}}$, $\rho_{r,r'''}$, $\rho_{r,\theta_{120}}$); 180° triplet collinear configurations and third shell defined only by $\sigma^2_{\theta_{180}}$ and $\rho_{r,r'^v}$, and the nonstructural $E_0$ and $S_0^2$ parameters. We assume a negligible skewness for the distribution of the shells beyond the first one. This is also supported by structural analysis of the results of the MC simulations presented in Sec. V.

The dominant contribution is the first-neighbor two-atom signal even at very high pressures, due also to the relatively large structural disorder. As a consequence, EXAFS structural refinement is particularly accurate for the shape of the first-neighbor distribution and we shall report only about the three parameters $R$, $\sigma^2$, and $\beta$.

The result of the fitting, in the case of solid krypton at 8 GPa, is shown in $k$ space in Fig. 7. The calculated signals are shown in the upper part of the figure (solid lines). The dominant low-frequency first-neighbor two-body $\gamma_1^{(2)}$, the three-body (60°) $\gamma_1^{(3)}$, the combined three-body (90, 120, 180°), and two-body (second, third, and fourth shell) $\eta_2^{(3)}$, $\eta_3^{(3)}$, and $\eta_4^{(3)}$ contributions are shown from the top to the bottom. In the lower part of the figure the total model signal (continuous line) and the experimental EXAFS (dots) are compared. The agreement between calculated and experimental signals is excellent.

The trend of the EXAFS spectra as a function of pressure is shown in Fig. 8, where experimental data recorded at 1.5

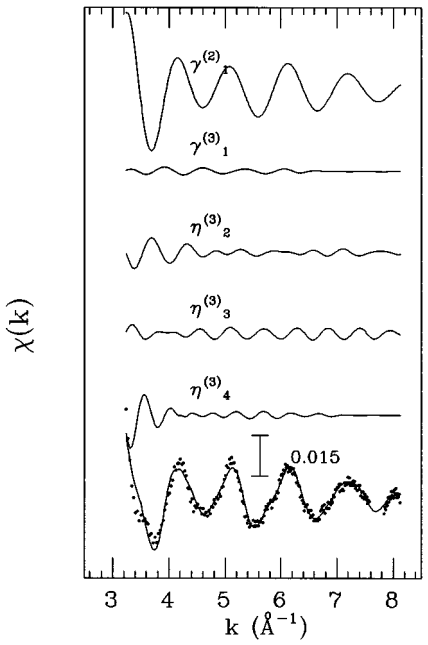


FIG. 7. Best fit of the EXAFS spectrum of solid krypton at 8 GPa and room temperature: theoretical $\chi(k)$ signals corresponding to pair and triplet configurations are reported as solid lines. In the lower part, the comparison between the total theoretical (continuous line) and the experimental spectrum (dots) is shown.

(3), 3.0 (3), 8.0 (3), 12.8 (5), and 29 (1) GPa are compared with best-fit multiple-scattering calculations. Agreement between calculated and experimental signals is good in the whole pressure and energy range.

EXAFS structural results related to the first-neighbor dis-

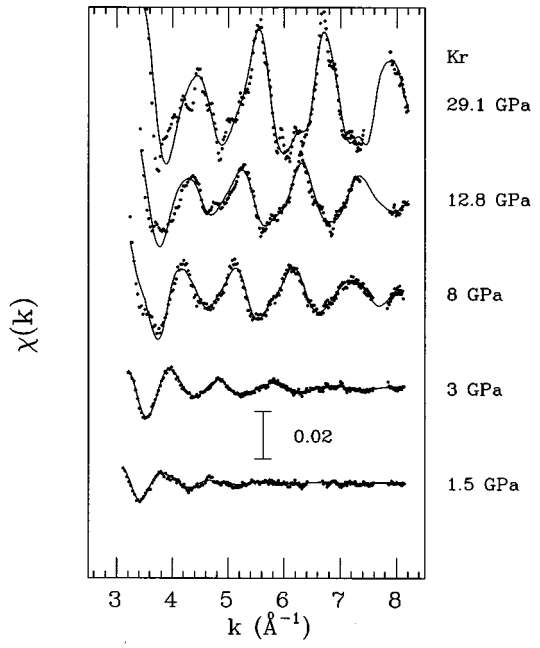


FIG. 8. EXAFS $\chi(k)$ spectra of solid krypton (dots) at 1.5, 3, 8, 12.8, and 29.1 GPa (room temperature) compared with best-fit multiple-scattering calculations (solid lines). Data containing Bragg peaks coming from the diamond-anvil cell are not shown.

TABLE III. First-shell parameters $R$, $\sigma^2$, and $\beta$ as determined by EXAFS for solid krypton at room temperature as a function of pressure.

| $P$ (GPa) | $R$ (Å) | $\sigma^2$ ($10^{-3}$ Å$^2$) | $\beta$ |
|---|---|---|---|
| 29(1) | 3.07(3) | 10(1) | 0.3(1) |
| 23(1) | 3.15(3) | 12(1) | 0.3(1) |
| 18.4(5) | 3.21(3) | 15(1) | 0.3(1) |
| 12.8(5) | 3.28(3) | 17(2) | 0.4(1) |
| 8.0(3) | 3.38(2) | 23(2) | 0.4(1) |
| 4.0(3) | 3.53(2) | 36(4) | 0.5(1) |
| 3.0(3) | 3.61(3) | 50(5) | 0.4(1) |
| 1.5(3) | 3.84(5) | 85(8) | 0.6(1) |

tribution are reported in Table III and compared with those obtained by MC simulations in Fig. 9. The results are particularly interesting. The overall trend as a function of pressure is in qualitative agreement with that of the Monte Carlo simulations. EXAFS best-fit parameters $R$, $\sigma^2$, and $\beta$ of solid krypton at pressures lower than 10 GPa are in quantitative agreement with those obtained using Monte Carlo simulations with the HFD-B (Ref. 2) potential.

In Fig. 9(a) the average bond-length $R$ values determined by EXAFS data analysis are compared with the results of the MC simulations as a function of pressure. At low pressures, the average bond-length $R$ is slightly longer than that predicted by the simulations, as also suggested by x-ray diffraction.[39] The slight elongation of the average bond length at very low pressures is assigned to the effect of higher-order interactions (see Sec. V). In the high-pressure range the average bond lengths measured by EXAFS ( $\diamond$ ) are in substantial agreement with those predicted by MC simulations and determined by x-ray-diffraction measurements [see Fig. 9(a)].

The bond distance variance differs for the two models,

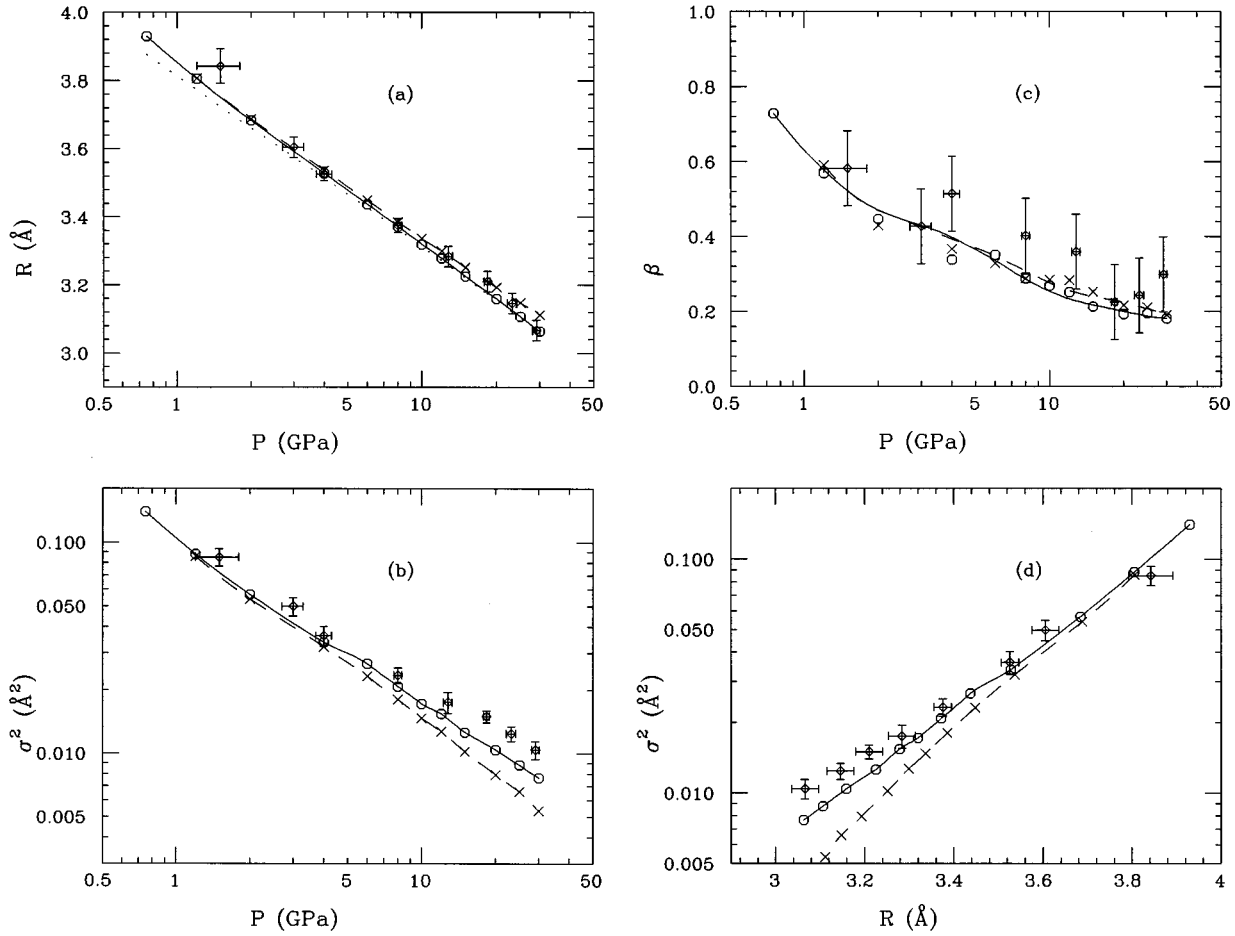


FIG. 9. Parameter of the first-neighbor distribution as a function of pressure. (a) The average bond length $R$ in fcc Kr is reported for the HFD-B (Ref. 2) ($\bigcirc$) and K2 (Ref. 1) ($\times$) potentials. The dotted line refers to the crystallographic value $a/\sqrt{2}$ (HFD-B only). The small deviation at low pressure indicates the effect of tangential vibrations. Best-fit bond lengths $R$ derived from EXAFS data ( $\diamond$ ) are shown with their error bar. (b) The bond distance variance $\sigma^2$ is shown in logarithmic scale as a function of pressure for the two potentials. EXAFS data are shown ( $\diamond$ ) in the same scale. (c) Skewness parameter $\beta$ as a function of pressure. Although the skewness parameter is determined with a large statistical error, the presence of an increasing asymmetry by lowering the pressure is quite evident. (d) Bond distance variance $\sigma^2$ as a function of the average bond length $R$ in various conditions of pressure for the two potentials and for the experimental EXAFS data ( $\diamond$ ). The slightly softer repulsive part of the HFD-B (Ref. 2) potential is reflected by the larger values of the bond variance for short distances (high pressures). EXAFS data indicate that the short-range part of the effective interatomic potential is slightly softer than that predicted by the HFD-B (Ref. 2) potential. The sensitivity of the EXAFS data to the short-range part of the potential can be appreciated.

especially at very high pressures. This is again a consequence of the different hard-core repulsive part of the two potentials. EXAFS data shown in Fig. 9(b), follow basically the curve obtained using the HFD-B potential up to 10–15 GPa and, at very high pressures (15–30 GPa), the experimental bond distance variances are found to be larger than those predicted by the MC simulations. The discrepancy with the results obtained using the K2 potential is larger at very high pressures, the experimental bond variance at 30 GPa is found to be two times larger than expected using the K2 potential. The bond distance variance probed by EXAFS contains important information about the shape of the interatomic potential which is not contained in diffraction data. In the present case, the hard-core repulsive part of the effective interaction potential is suggested to be softer than that of both pair interaction models. Notice that quantum corrections to the present classical simulation are at least one order of magnitude smaller than the observed differences. In the worst case, the classical simulation with the HFD-B potential at 30 GPa gives $\sigma^2 \sim 0.0076$ Å$^2$ which corresponds to an effective Kr-Kr bond stretching frequency of about 150 cm$^{-1}$. For an harmonic oscillator the difference between classical and quantum treatments is in this case less than 0.0002 Å$^2$.

In Fig. 9(c), the skewness parameter $\beta$ is reported as a function of pressure. The presence of an increasing asymmetry by lowering the pressure, predicted by both HFD-B and K2 models, is quite evident also in the EXAFS data, although the statistical error is large.

Results on bond distances $R$ and variances $\sigma^2$ are reported in a single comprehensive plot in Fig. 9(d), which does not depend on the accuracy of the pressure scale. The $\sigma^2$ value for a given $R$ measures the softness of the interaction as a function of the average distance and provides a unique insight on the shape of the interaction with a single measurement.

In Fig. 9, the difference between the results of the simulations with the K2 or HFD-B pair potentials is due to the slightly softer repulsive part of the HFD-B potential. Differences are sometimes very large, especially at high pressures, indicating the high sensitivity of these EXAFS observables to the short-range details of the interaction. Comparison with EXAFS data indicates that the short-range part of the effective interatomic potential is slightly softer than that of the HFD-B (Ref. 2) potential. Differences between experimental results and simulation with pair potentials can also be produced by the many-body interactions that are neglected. The structural results reported in Fig. 9 clearly show the usefulness of EXAFS measurements for investigating atomic interaction properties in condensed matter.

## VII. EXAFS OF LIQUID KRYPTON

The EXAFS spectrum of liquid krypton has been calculated starting from the results of the Monte Carlo simulations presented in Sec. V according to the expression[28]

$$\langle \chi(k) \rangle = \int_0^\infty dr 4\pi r^2 \rho g(r) \gamma^{(2)}(r,k), \qquad (12)$$

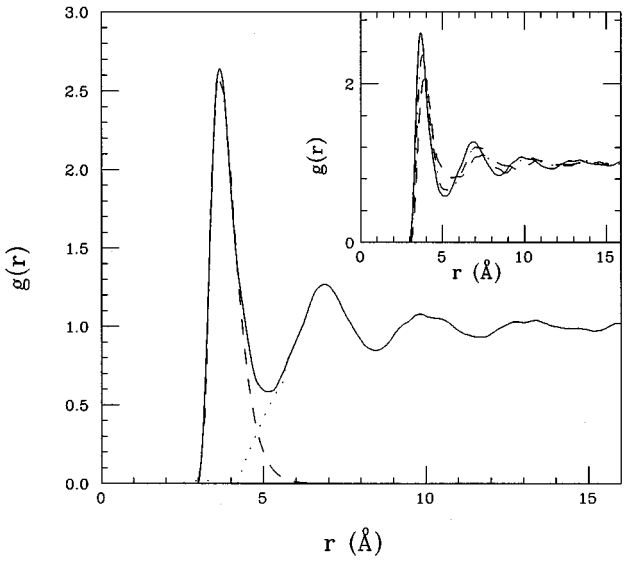


FIG. 10. Pair-distribution function $g(r)$ of liquid krypton at $T=300$ K and $P=0.75$ GPa as determined by Monte Carlo computer simulations using the HFD-B (Ref. 2) potential. Dashed and dotted curves are the decomposition of the $g(r)$ into the first-neighbor peak and a long-range tail, respectively. The trend of the $g(r)$ as a function of pressure is shown in the inset for $P=0.1$ GPa (dot-dashed), $P=0.35$ GPa (dashed), and $P=0.75$ GPa (solid).

where only the two-body term has been retained in the evaluation of the measured $\chi(k)$ signal.

In Fig. 10 we show the pair-distribution function $g(r)$ of liquid krypton at $T=300$ K and $P=0.75$ GPa as determined by Monte Carlo computer simulations using the HFD-B (Ref. 2) potential starting from random initial conditions. The trend of the $g(r)$ of liquid krypton as a function of pressure is shown in the inset of the same figure for $P=0.1$ GPa (dot-dashed curve), $P=0.35$ GPa (dashed curve), and $P=0.75$ GPa (solid curve).

Due to the short-range nature of the $\gamma^{(2)}(r,k)$ function, the $\chi(k)$ signal obtained by direct application of Eq. (12) is mainly sensitive to the shape of the first peak of the $g(r)$. In Fig. 10 a convenient decomposition of the $g(r)$ into a well-defined short-range peak (dashed) and a long-range oscillatory tail (dots) is reported.[43–45] The averaged $\gamma^{(2)}(k)$ signals associated with the first peak and the tail of the $g(r)$ has been calculated and compared with the experimental EXAFS signal.

In Fig. 11 we report the comparison between the EXAFS spectrum of liquid krypton at 0.75 GPa and room temperature calculated starting from the $g(r)$ obtained from MC simulations (shown in Fig. 10) and that measured using the dispersive setup. The upper curves are the calculated $\gamma^{(2)}(k)$ signals associated with the first peak of the $g(r)$ and with the long-range oscillatory tail. It is clear that the EXAFS $\chi(k)$ pattern is dominated by the signal associated with the first peak of the $g(r)$. The resulting $\chi(k)$ signal is however very weak (of the order of 0.001) and therefore low-noise EXAFS measurements of liquid krypton are needed to detect the structural signal. The EXAFS pattern of our best measurement of liquid krypton at a pressure of 0.75 GPa and room temperature is reproduced within the noise by the calculated $\chi(k)$, as also shown by the residual (lower

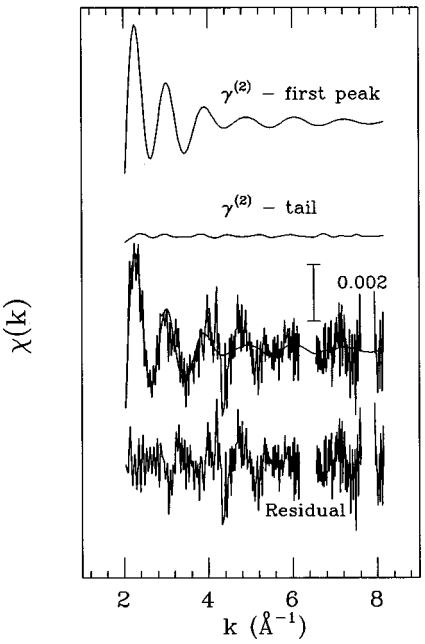


FIG. 11. Comparison between the EXAFS spectra of liquid krypton at 0.75 GPa and room temperature measured using the dispersive setup and calculated staring from the $g(r)$ obtained from MC simulations (see Fig. 10). The upper curves are the calculated $\gamma$ signals associated with the first peak of the $g(r)$ and with the long-range oscillatory tail. The resulting EXAFS signal is very weak (of the order of 0.001). The total signal (continuous line), dominated by the first-neighbor contribution, reproduces within the statistical errors the superimposed experimental data, as also shown by the residual (lower curve).

curve in Fig. 11). The quality of the present data and the weak amplitude of the structural signal do not allow us to attempt a refinement of the short-range $g(r)$ in liquid Kr, as it has been done for other liquid systems.[44–46] However, present EXAFS data are consistent with MC simulations based on the HFD-B potential.

## VIII. CONCLUSIONS

A detailed investigation of the high-pressure $K$-edge x-ray-absorption spectra of solid and liquid krypton has been carried out. Near-edge structures have been accurately studied as a function of pressure by means of multiple-scattering calculations. The appearance of the white line and its trend for increasing pressure has been interpreted as due to a multiple-scattering resonance just above the $K$ threshold. Due to the feeble intensity of the EXAFS structural signal at low pressures, the edge features are the most sensitive signatures for local ordering in condensed krypton, and are mainly related to the first-neighbor interatomic distance. It has been shown that the near-edge structures are reproduced taking into account two-body and three-body terms associated with the first-neighbor shell.

EXAFS (extended x-ray absorption fine-structure) data analysis has been carried out using the advanced GNXAS multiple-scattering method taking proper account of the atomic background including the $[1s4p]$, $[1s3d]$ and $[1s3p]$ double-electron excitation channels, for which specific measurements have been performed. A deep insight on the local structure of condensed krypton at high pressures has been gained by comparing EXAFS results with constant pressure Monte Carlo computer simulations based on well-known empirical pair potentials proposed by Barker (K2) and Aziz (HFD-B). EXAFS data have been found to be particularly sensitive to the details of the first-neighbor distribution, described by the average bond-length $R$, the bond distance variance $\sigma^2$ and the skewness $\beta$.

Differences in the first-neighbor distribution derived using either the K2 or the HFD-B potentials are found in solid krypton especially at high pressures, due to the different shape of the hard-core repulsive part of the two potentials. Quantitative agreement between EXAFS results and MC simulations using the HFD-B potential has been obtained at moderate pressures. Slight deviations from the results of the simulations have been found at high pressures. EXAFS data at high pressures are in better agreement with the trend obtained using the HFD-B potential, than with the results of the simulations based on the K2 potential. Present results on high-pressure solid krypton suggest the existence of a softer hard-core repulsive part for the potential. At low pressures, the EXAFS signal of liquid krypton at room temperature and 0.75 GPa has been found in accord with the results of the MC simulations within the noise of the measurement. However, the quality of the data and the intrinsic weak amplitude of the EXAFS signal in liquid krypton hampered us to obtain a reliable refinement of the short-range structure.

The whole body of the results reported in this paper indicates that the use of the x-ray absorption spectroscopy is potentially very important in the study of matter in extreme conditions such as high pressures. In fact, the availability of intense and brilliant synchrotron radiation sources and the development of specific techniques for the measurement of liquid and solid materials in extreme high-pressure and/or high-temperature conditions makes the access to XAS experiments easier and more attractive than before. Moreover, the development of accurate and reliable data-analysis methods allowed us to obtain results in quantitative agreement with computer simulations in solid and liquid krypton as well as in other cases presented elsewhere. In this way, XAS results can nicely complement those of the diffraction techniques and can be useful to refine the short-range structure of condensed systems in extreme conditions. While diffraction techniques are certainly necessary to study the medium and long-range correlations, XAS can be more sensitive and accurate in the determination of the short-range structure in ordered and disordered systems. The example presented in this paper shows that a XAS experiment can provide a deep insight into the nature of the microscopic interactions in condensed matter in a textbook case (solid krypton) and in particular the direct measurement of length scale and vibrational parameters provide a unique test for the potential models in the high-pressure regime.

## ACKNOWLEDGMENTS

A.D.C. is grateful for the friendly hospitality of the LURE staff during his stay.

[1] J. A. Barker, R. O. Watts, J. K. Lee, T. P. Schafer, and Y. T. Lee, J. Chem. Phys. **61**, 3081 (1974).
[2] R. A. Aziz and M. J. Slaman, Mol. Phys. **58**, 679 (1986).
[3] B. M. Axilrod and E. Teller, J. Chem. Phys. **11**, 299 (1943); Y. Muto, Proc. Phys. Math. Soc. Jpn. **17**, 629 (1943).
[4] A. Teitsma and P. A. Egelstaff, Phys. Rev. A **21**, 367 (1980).
[5] P. A. Egelstaff, A. Teitsma, and S. S. Wang, Phys. Rev. A **22**, 1702 (1980).
[6] G. C. Aers and M. W. C. Dharma-wardana, Phys. Rev. A **29**, 2734 (1984).
[7] J. A. Barker, Phys. Rev. Lett. **57**, 230 (1986).
[8] H. Fredrikze, Phys. Rev. A **36**, 2272 (1987).
[9] F. Barocchi, P. Chieux, R. Magli, L. Reatto, and M. Tau, Phys. Rev. Lett. **70**, 947 (1993).
[10] F. Barocchi, P. Chieux, R. Magli, L. Reatto, and M. Tau, J. Phys. Condens. Matter **5**, 4299 (1993).
[11] F. Barocchi, P. Chieux, and R. Magli, J. Phys. Condens. Matter **5**, B49 (1993).
[12] L. Reatto and M. Tau, J. Chem. Phys. **86**, 6474 (1987).
[13] M. Breining, M. H. Chen, G. E. Ice, F. Parente, and B. Crasemann, Phys. Rev. A **22**, 520 (1980).
[14] M. Deutsch and M. Hart, Phys. Rev. Lett. **57**, 1566 (1986); Phys. Rev. A **34**, 5168 (1986).
[15] E. Bernieri and E. Burattini, Phys. Rev. A **35**, 3322 (1987).
[16] Y. Ito, H. Nakamatsu, T. Mukoyama, K. Omote, S. Yoshikado, M. Takahashi, and S. Emura, Phys. Rev. A **46**, 6083 (1992).
[17] S. J. Schaphorst, A. F. Kodre, J. Ruscheinski, B. Crasemann, T. Åberg, J. Tulkki, M. H. Chen, Y. Azuma, and G. S. Brown, Phys. Rev. A **47**, 1953 (1993).
[18] J. A. Soules and C. H. Shaw, Phys. Rev. **113**, 470 (1959).
[19] F. W. Kutzler, D. E. Ellis, T. I. Morrison, G. K. Shenoy, P. J. Viccaro, P. A. Montano, E. H. Appelman, L. Stein, M. J. Pellin, and D. M. Gruen, Solid State Commun. **46**, 803 (1983).
[20] A. Polian, J. P. Itié, E. Dartyge, A. Fontaine, and G. Tourillon, Phys. Rev. B **39**, 3369 (1989).
[21] C. A. Guryan, K. B. Lee, P. W. Stephens, A. I. Goldman, J. Z. Larese, P. A. Heiney, and E. Fontes, Phys. Rev. B **37**, 3461 (1988).
[22] Z. Tan, J. I. Budnick, D. M. Pease, and F. Namavar, Phys. Rev. B **43**, 1987 (1991).
[23] I. Kwon, L. A. Collins, J. D. Kress, and N. Troullier, Phys. Rev. B **52**, 15 165 (1995).
[24] E. Dartyge, C. Depautex, J. M. Dubuisson, A. Fontaine, A. Jucha, and G. Tourillon, Nucl. Instrum. Methods Phys. Res. Sect. A **246**, 452 (1986).
[25] H. K. Mao, P. M. Bell, J. W. Shaner, and D. J. Steinberg, J. Appl. Phys. **49**, 3276 (1978).
[26] R. K. Crawford and W. B. Daniels, J. Chem. Phys. **55**, 5651 (1971).
[27] T. A. Tyson, K. O. Hodgson, C. R. Natoli, and M. Benfatto, Phys. Rev. B **46**, 5997 (1992).
[28] A. Filipponi, A. Di Cicco, and C. R. Natoli, Phys. Rev. B **52**, 15 122 (1995).
[29] A. Filipponi, J. Phys. Condensed Matter **3**, 6489 (1991).
[30] L. Hedin and B. I. Lundqvist, J. Phys. C **4**, 2064 (1971).
[31] C. R. Natoli, *Proceedings of the International Conference on EXAFS and Near-Edge Structure, Frascati, Italy*, edited by A. Bianconi, L. Incoccia, and S. Stipcich, Springer Series in Chemical Physics Vol. 27 (Springer-Verlag, Berlin, 1983).
[32] M. O. Krause and J. H. Oliver, Phys. Chem. Ref. Data **8**, 329 (1979).
[33] A. Filipponi, Physica B **208 & 209**, 29 (1995).
[34] J. Desclaux, Comp. Phys. Commun. **9**, 31 (1975); J. Phys. B **4**, 631 (1971).
[35] A. Filipponi and A. Di Cicco, Phys. Rev. A **52**, 1072 (1995).
[36] A. Di Cicco and A. Filipponi, Phys. Rev. B **49**, 12 564 (1994).
[37] I. R. McDonald, Mol. Phys. **23**, 41 (1972).
[38] N. J. Trappeniers, T. Wassenaar, and G. J. Wolkers, Physica **32**, 1503 (1966).
[39] A. Polian, J. M. Besson, M. Grimsditch, and W. A. Grosshans, Phys. Rev. B **39**, 1332 (1989).
[40] I. V. Aleksandrov, A. N. Zisman, and S. M. Stishov, Sov. Phys. JETP **65**, 371 (1987).
[41] A. Filipponi, A. Di Cicco, T. A. Tyson, and C. R. Natoli, Solid State Commun. **78**, 265 (1991).
[42] A. Filipponi and A. Di Cicco, Phys. Rev. B **52**, 15 135 (1995).
[43] A. Filipponi, J. Phys. Condensed Matter **6**, 8415 (1994).
[44] A. Filipponi and A. Di Cicco, Phys. Rev. B **51**, 12 322 (1995).
[45] A. Di Cicco, Phys. Rev. B **53**, 6174 (1996).
[46] A. Di Cicco and A. Filipponi, Europhys. Lett. **27**, 407 (1994).